AIAA JOURNAL
Vol. 46, No. 6, June 2008

Aerodynamics of a Flapping and Pitching Wing Using Simulations and Experiments

K. M. Isaac* and Jessica Rolwes†
Missouri University of Science and Technology, Rolla, Missouri 65409
and
Anthony Colozza‡
NASA John H. Glenn Research Center at Lewis Field, Cleveland, Ohio 44135

DOI: 10.2514/1.32846

Computational fluid dynamics simulation results for a thin cambered plate airfoil, and flow visualization and force measurements from experiments conducted in water on a flapping-and-pitching thin flat-plate wing of semi-elliptic planform at low Reynolds numbers are reported. Time-varying force data, measured using a force transducer, provide a means to understand the mechanisms that lead to enhanced performance observed in insect flight compared with fixed-wing aerodynamics. Experimental uncertainties associated with low-level (∼1 N) fluid dynamic force measurements on flapping-and-pitching wings, including inertia effects, are addressed. A previously proposed pitching mode in which the leading-edge and trailing-edge switch roles to allow using cambered airfoils is shown to be feasible. A vortex-trapping model is proposed to explain the aerodynamic advantages of switching. The present results also support the authors' proposed idea that an optimum reduced flapping frequency might exist. The study has applications in micro air vehicle development.

Nomenclature

A = wing cross-sectional area
C_L = wing lift coefficient
c = chord length
c_1 = airfoil lift coefficient
D = drag force
F = force
f = frequency
h = depth
k = reduced frequency
L = lift force
l_c = hinge-to-midspan distance
l_w = wing length
P = force
$\bar{q}$ = $\rho\bar{U}^2/2$
Re_c = chord Reynolds number ($=\bar{U}c/\nu$)
S = wing planform area
St = Strouhal number
s = strain gauge spacing
U = velocity
$\bar{U}$ = cycle average speed at midspan ($=2l_c\psi f$)
Δt = time increment
α = angle of attack
γ = stroke plane inclination
λ = wave length
ν = kinematic viscosity
ξ = angular displacement
ρ = fluid density
τ = period
τ_s = servo rotation time ($2\alpha/\omega_s$)
ψ = stroke angle
ω = $2\pi f$
ω_s = Servo angular velocity

Introduction

INVESTIGATION of low Reynolds number flapping wings has picked up momentum lately because of the potential applications in micro air vehicles. The authors and their coinvestigators studied two such candidate vehicles for planetary exploration and terrestrial applications, and the results have been reported [1,2]. These studies emphasized the vehicle as a system from the point of view of its payload, aerodynamics, materials, propulsion, control, navigation, and communication. The studies concluded that flapping-wing aerodynamics have many desirable features such as providing thrust and lift forces from the same source and the ability to integrate all the subsystems into a solid state aircraft. These studies also concluded that vehicle development will require further research on the subsystems. The present work is a continuation of these efforts to better understand insect flight mechanisms and incorporate their desirable features into micro air vehicle (MAV) development.

Insects generate thrust and lift by controlling wing kinematics that include flapping and pitching during the stroke cycle. Other mechanisms, such as camber control, wing flexure, forewing–hindwing coordination, and variation of stroke plane inclination, have also been observed. Insect aerodynamics have been investigated largely by two groups: biologists and aerodynamicists. Many published reviews cover flapping-flight aerodynamics from various angles. There exists a large body of experimental work on insect aerodynamics; though they provide good qualitative descriptions, because of the difficulties associated with doing experiments on small live animals, the reported quantitative results are often incomplete and have large experimental error bands.

Many aspects of fixed and flapping MAV are covered in a recent compilation of papers by many researchers [3]. Mueller and DeLaurier recently reviewed various aspects of MAV aerodynamics [4]. Sane reviewed insect flight aerodynamics highlighting its unique aspects [5]. Ellington [6] and Usherwood and Ellington [7] studied the novel aspects of insect flight with the goal of incorporating them in micro air vehicle design. To provide basic steady state aerodynamic characteristics, Torres and Mueller recently conducted experimental investigation of low Reynolds number, low-aspect-ratio, flat-plate

Presented as Paper 0450 at the Aerospace Sciences Meeting, Reno, NV, 9–13 January 2006; received 16 June 2007; revision received 30 December 2007; accepted for publication 6 February 2008.

*Professor, Mechanical and Aerospace Engineering, 1870 Miner Circle. Associate Fellow AIAA.
†Graduate Assistant, Mechanical and Aerospace Engineering, 1870 Miner Circle.
‡Project Engineer, Mail Stop 301-3.

wings [8]. Vortical signatures of heaving and pitching airfoils were investigated by Freymuth [9], who observed a reverse Karman vortex street that resulted in thrust production. Gopalkrishnan et al. [10] investigated a plunging-and-pitching foil in a cylinder wake. Different modes of interaction of the foil with the cylinder wake are described. Anderson et al. [11] conducted a systematic investigation of thrust-producing mechanisms of harmonically oscillating foils in a steady freestream flow by flow visualization at $Re = 1100$ and by force measurements at $Re = 40,000$. Lewin and Haj-Hariri [12,13] studied thrust generation of a heaving airfoil. Koochesfahani [14] also examined the vortical pattern in the wake-and-thrust generation.

Dickinson et al. [15] examined various aspects of wing kinematics and proposed the "delayed-stall-rotational-lift-wake-capture" mechanism to explain lift generation during all phases of the wing beat cycle. Tarascio et al. [16] experimentally visualized leading-edge vortices (LEVs) shed from insectlike flapping wings in air. Vest and Katz [17] used a panel method to investigate unsteady aerodynamics of model flapping wings. Ramamurti and Sandberg [18] conducted numerical simulation using the Euler equations and compared their results with those of flat-plate wing experiments of Dickinson et al. [15].

The authors' computational fluid dynamics (CFD) simulations of cambered plate airfoils [19] helped establish the relationship between the Strouhal number of the Karman vortex street and the reduced frequency of flapping that leads to optimum lift production. Even though a CFD study of the wing that includes the flapping-and-pitching motions and viscous effects might be more desirable, the necessary CFD tools that will provide reliable quantitative results for such a complex flowfield are still being developed. The authors' observations relating their unsteady flow-simulation results, including the leading-edge and trailing-edge vortex dynamics, of a stationary two-dimensional airfoil to the flapping wing are strengthened by the recent works of Lentink and Gerritsma [20] and Taylor et al. [21]. They compiled the reduced frequency (k) of a large number of natural fliers and showed that it falls within a narrow band close to that of the Karman vortex street. Effects due to finite span and wing kinematics are also bound to have an influence on the optimum reduced frequency observed in natural fliers. The authors' subsequent experiments on flapping-and-pitching (see Figs. 1 and 2 for related axes description) wings provided force data and flowfield information [22,23]. Based on the cyclical lift variation and the leading-edge/trailing-edge vortex dynamics from their CFD simulations, they also suggested a "leading-edge/trailing-edge" (LE/TE) switching mode to take advantage of the trailing-edge vortex to enhance lift and explained lift augmentation with the help of a vortex-trapping model.

Flapping-and-Pitching Motion

To make subsequent discussions of the experimental results clear, we begin with a detailed description of the wing motion. Figure 1 shows two orthogonal coordinate systems, inertial (XYZ) and wing fixed (xyz), that are helpful to understand the wing motion. For flapping, the spanwise axis (y axis) sweeps in the XY plane about the Z axis with a sweep angle ψ. All the experiments were done in a symmetric pitching mode, namely, half the pitching displacement takes place before reaching the end of stroke and the other half after. To orient the reader toward a clear understanding of the kinematics, a chord line AB with the filled circle at one end, is shown in Figs. 1–3. Figure 1 shows the two coordinate systems and the angles ξ and ψ that lie in the stroke plane XY. Figure 2 gives an overview of the experimental setup. Figure 3 shows the chord line in end view at various instants during the downstroke and the upstroke, each with a time duration of $\tau/2$. The servo trigger times and the different orientations of the line AB when the servo and the wing are rotating can also be seen in Fig. 3. τ_s denotes the time for servo rotation through angle 2α. When the spanwise axis (y axis) is exactly at the end of the stroke shown in Fig. 1, the chord line AB lies in the XY plane. Note in Fig. 3 that edge B is the leading edge during the downstroke, and edge A is the leading edge during the upstroke. We call this the leading-edge/trailing-edge switching mode.

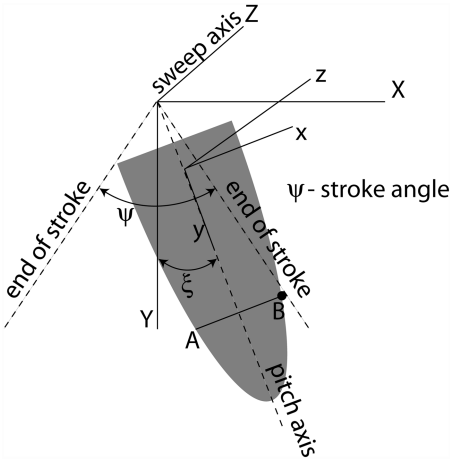

Fig. 1 Coordinate systems used to describe wing motion. The pitch axis y sweeps in the XY plane of the inertial XYZ system, whereas the wing pitches about the y axis of the wing-fixed xyz system. The chord line AB is also shown in Figs. 2 and 3.

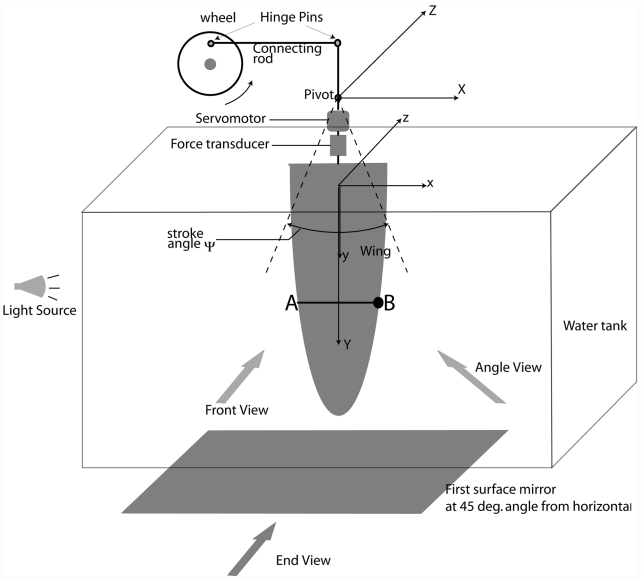

Fig. 2 Schematic diagram of the experimental setup. The two coordinate systems XYX and xyz are also shown. Note that the coordinate systems and the chord line AB correspond to those in Fig. 1.

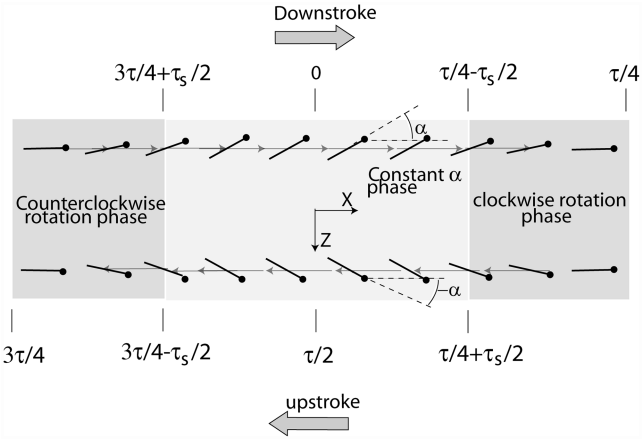

Fig. 3 Wing in downstroke and upstroke. The line with the black dot at the tip represents the chord line (AB) shown in Figs. 1 and 2. The motion is as seen in end view, Fig. 2. The constant angle-of-attack phase is in lighter gray, and the two rotational phases, one clockwise (CW) and the other counterclockwise (CCW), are shown in darker gray.

Two-Dimensional Simulations

A circular arc airfoil with the following geometric details was used: chord length = 50 mm, maximum camber = 0.5 mm (1%), and constant thickness = 2.5 mm (5%). The leading edge and trailing edge are rounded using semicircular arcs. The simulations are for the unsteady viscous flow over the stationary airfoil in a steady freestream flow. The flow unsteadiness arises from the vortex shedding.

The FLUENT [24] numerical simulation package has many options for space and time discretization. For the present laminar flow case, all the available space discretization schemes could be used without perceptibly influencing the solution. For space discretization, the second-order upwind scheme [25] was chosen. The equations are solved sequentially: first the momentum equations, and then the conservation of mass equation. A point-implicit linear-equation solver is used in conjunction with an algebraic multigrid method to solve the resultant scalar system of equations. Most of the results presented in this paper are based on an unsteady, first-order implicit method for time discretization. The discretization in the general form for variable ϕ is as follows:

$$\frac{\phi^{n+1} - \phi^n}{\Delta t} = F(\phi^{n+1}) \tag{1}$$

where n represents the time level and Δt represents the time step size. The second-order accurate implicit form for time discretization, used in selected cases to establish numerical accuracy, is given by

$$\frac{3\phi^{n+1} - 4\phi^n + \phi^{n-1}}{2\Delta t} = F(\phi^{n+1}) \tag{2}$$

The computational domain with a parabolic inflow boundary and planar outflow boundary extended approximately 10 chord lengths to the front, rear, top, and bottom. The production runs employed $\sim$160,000 quadrilateral cells finely distributed close to the airfoil surface and coarser toward the outer boundaries. Before the production runs, the grid quality was checked using several criteria [19].

The numerical schemes available in the software package used in the present study have been used in numerous other studies, including those by the present authors, and their behavior such as numerical diffusion has been well documented. Therefore, code validation for the present work focused mainly on validating the procedures relevant to the present work. As a part of this effort, flow simulation of an NACA 0012 airfoil at low angle of attack and high Reynolds number was done, and the lift curve was compared with published airfoil data. The comparison showed excellent agreement. Code validation for airfoil type problems has also been done in our earlier work, and the results have been documented. Additionally, one case was run with three segments, each for 2.5 s of flow time. Second-order implicit scheme with step size $\Delta t = 0.001$ s was used in the first segment. For the second segment, the time integration scheme was changed to first-order implicit, and for the third segment, first-order implicit scheme was used with the step size halved to 0.0005 s. The lift curves from these runs showed no discernible effects due to the previously described choices [19], indicating that the results are not influenced by the choice of the numerical integration scheme or the selected step sizes.

With the help of the two-dimensional simulation results given in Figs. 4–6, the flowfield was analyzed, and the phase relations of the leading-edge/trailing-edge vortex (LEV/TEV) dynamics to cyclical lift variation were established. The results show the fixed wing undergoing a high-lift phase during each lift cycle. At moderately high $\alpha(\leq 20$ deg), the LEV dominates, and as α increases, the TEV plays an increasing role in the vortex dynamics. The Strouhal number for all the cases considered was close to that of the Karman vortex shedding. It is interesting to note that the lift curve from our work is very similar to that of Cloupeau et al. [26]. These observations led us to propose that, by matching the reduced beat frequency of flapping to the near-constant Strouhal number of Karman vortex shedding, the wing can avoid operating in the low lift phase, explaining, at least in part, the high lift associated with insect flight. Analysis of flight data of a large number of insects [20,21] showed that their reduced beat frequencies indeed lie in a narrow band close to the Strouhal number of Karman vortex shedding.

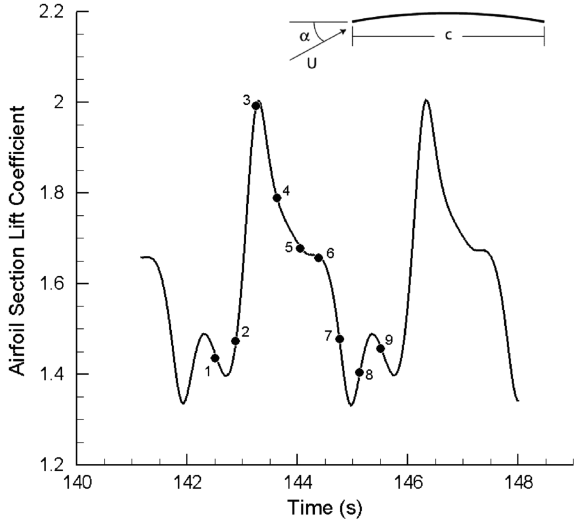

Fig. 4 Unsteady lift coefficient from simulation results of a stationary cambered plate airfoil in steady freestream flow (see inset). The numbers by the filled circles on the c_1 curve correspond to the nine pressure contour frames captured sequentially at nine instants during the lift cycle shown in Fig. 5. The nine filled circles are spaced at a time interval $\Delta t = 375$ ms.

To establish the phase relationship between the c_1 variation and the dynamics of the LEV/TEV, results from one case are presented in Figs. 5 and 6. The corresponding chord Reynolds number is 500, and the angle of attack is 29.4 deg. For one cycle, the c_1 curve (Fig. 4) spans a period of $\tau \approx 3$ s. The Strouhal number can be calculated as 1) $St_A = fc/U_\infty$ or 2) $St_B = fc\cos\alpha/U_\infty$, where $c\cos\alpha$ is the projection of the chord line along the freestream velocity direction. Several important flow features can be discerned from these results. At this high α, the wing generates a large amount of lift, indicating that extrapolation of high Reynolds results would be erroneous; especially, the catastrophic stall pattern of conventional high Reynolds airfoils is not observed in the present cases. The other feature is the large amplitude of the c_1 oscillations with time. The frequency and amplitude of the lift and drag variations depend on α and Re_c.

Lift and drag coefficient variations for two values of α (44.2 and 29.4°) and five values of freestream velocity ranging from 0.14 m/s ($Re_c \approx 500$) to 1.4 m/s ($Re_c \approx 5000$) were plotted and analyzed [19]. This set of c_1 and c_d plots reveals several interesting characteristics of low-Reynolds, high-α aerodynamics. The plots (not reproduced here) show that there are distinct frequencies associated with each case, and both the lift and drag variations have fairly large amplitudes. The salient features are summarized in Table 1, which shows the Strouhal number calculated in two different ways. These results indicate that, for all these cases, the flow is dominated by the formation and shedding of the leading-edge/trailing-edge vortices (LEV/TEV) as indicated by the pressure contours given in Fig. 5 and the vorticity contours given in Fig. 6. Frames 2–4 show that the LEV forms at the leading edge, stays attached to the top surface, and grows as it convects downstream. Comparing the lift curve in Fig. 4 and the pressure contours in Fig. 5 shows that c_1 increases steeply between frames 2 and 3, the early stage in the evolution of the leading-edge vortex, and then the c_1 drops as the LEV begins to detach from the surface, leading to the low c_1 phase of the cycle. Notice that two TEVs are formed, a weak one in frame 5, Fig. 5, followed by the stronger one in frames 8 and 9. Frames 9 and 1 have nearly the same pressure contours, indicating that the cycle is beginning to repeat itself. This can also be seen in Fig. 4 in which points 1 and 9 on the lift curve are at corresponding points on the two lift cycles shown. The shoulder in Fig. 4 in the

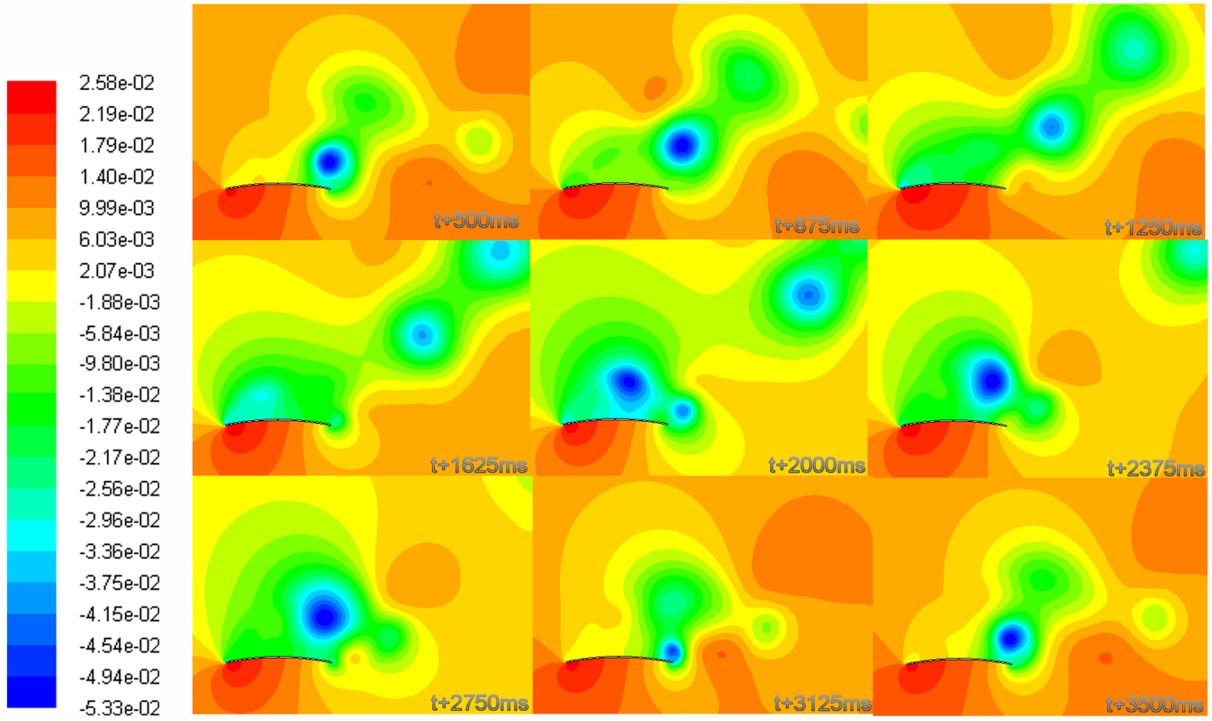

Fig. 5 Pressure contours from simulation results of a stationary cambered plate airfoil in steady freestream flow (see inset, Fig. 4). These nine frames are in the same order (earliest to latest) as the nine points shown in Fig. 4. These frames are 375 ms apart. $t = 142$ s. c_1 values corresponding to each frame can be read from Fig. 4.

region between points 4 and 6 is probably caused by the formation and detachment of the weaker TEV mentioned previously. The low c_1 phase continues during the formation, growth, and detachment of the stronger TEV. In general, the higher harmonics present in Fig. 4 can be attributed to weaker secondary vortices in addition to the one cited here. Because they are of low strength, some may be washed out and not visible in the nine frames in Fig. 5. The vorticity contours in Fig. 6, which correspond to the pressure contours in frame 9, Fig. 5, clearly show the sense of rotation of the LEV and TEV. At this instant, the TEV is about to detach from the trailing edge, and a new cycle is about to begin. Results [19] not presented here show that the c_d variation has a phase difference of approximately 180 deg from the c_1 variation.

From the summary results given in Table 1, several useful design guidelines can be drawn. Over the Reynolds number range considered, the Strouhal number (St_A) defined previously (second row from the bottom, Table 1) stays close to 0.22, the established value for Karman vortex shedding in bluff body flows at low Reynolds numbers [27]. The Strouhal number (St_B) based on the projected length has lower values as indicated by the last row in Table 1, and the difference between the two is larger at the higher angle of attack, a result of the $\cos\alpha$ factor in the St_B definition. Another important observation is that the cases in the Reynolds number range in Table 1 do not yield a steady state solution,

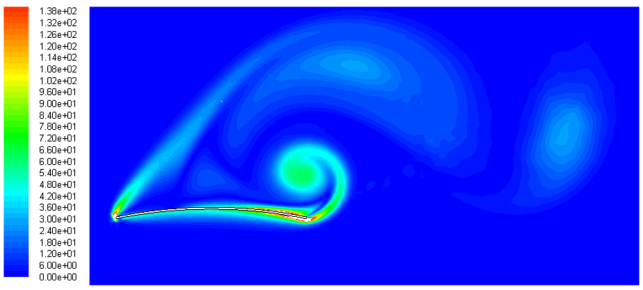

Fig. 6 Vorticity contours corresponding to the last frame in Fig. 5, as indicated by the time stamps. The detached leading-edge vortex and the trailing-edge vortex are clearly visible.

indicating that such a solution will violate the flow physics. A similar observation has also been made by Kunz and Kroo [28], and several others. Note that, for the Reynolds number range of this study, the flow cannot be approximated as being dominated by viscous forces, a valid assumption for $Re_c \ll 1$, nor can it be approximated as being dominated by inertia forces, a common assumption for $Re_c \gg 1$. For this reason, analytical results are not available in the literature for this flow regime.

If the wing-stroke-reduced frequency were to match the Strouhal number, the low c_1 phase can be avoided, and the airfoil can always stay in the high c_1 phase. In a practical design, this would require establishing the relationship between the flow velocity and the frequency of the LEV/TEV dynamics, so that, by choosing appropriate stroke cycle frequency, the wing would operate in the high c_1 mode during the entire cycle. The present results suggest that the ability to have variable beat frequency depending on flight conditions to improve performance should be a design goal. Formulating control laws that take into account these effects should, therefore, be part of designs based on this concept.

Scaling Parameters and Force Components

Two important nondimensional parameters, chord Reynolds number (Re_c) and reduced frequency (k), can be defined to study performance of a flapping wing. Because there is no freestream velocity for the hovering mode investigated in the present work, a cycle-averaged translational speed at the wing midspan $\bar{U}$ is used to express Re_c and k in terms of the chord length c, the distance from the hinge point to the wing midspan l_c, and the stroke angle ψ (Fig. 1). $\bar{U}$ can be expressed in terms of the wing beat frequency f as follows:

$$\bar{U} = 2l_c\psi f \tag{3}$$

A Reynolds number can be defined as

$$Re_c = \frac{\bar{U}c}{\nu} \tag{4}$$

Substituting for $\bar{U}$ from Eq. (3) gives the following for Re_c:

Table 1 Strouhal number from simulations. $St_A = fc/U_\infty$; $St_B = fc\cos\alpha/U_\infty$

Reynolds no.	510.00	1020.00	2040.00	3825.00	5100.00	510.00	1020.00	2040.00	3825.00	5100.00
Angle of attack, deg	44.20	44.20	44.20	44.02	44.20	29.40	29.40	29.40	29.40	29.40
Strouhal no., St_A	0.24	0.22	0.21	0.22	0.2	0.33	0.25	0.22	0.22	0.23
Strouhal no., St_B	0.17	0.15	0.15	0.15	0.14	0.16	0.12	0.11	0.11	0.11

$$Re_c = \frac{2l_c\psi fc}{\nu} \tag{5}$$

The reduced frequency is defined in terms of the wing beat frequency f as

$$k = \frac{fc}{\bar{U}} \tag{6}$$

Combining this expression with Eq. (3) yields the following:

$$k = \frac{c}{2l_c\psi} \tag{7}$$

Note that the wing beat frequency f does not appear explicitly in Eq. (7) for the reduced frequency. For a given wing assembly, it varies inversely as the stroke angle. Re_c is proportional to the product of stroke angle and the beat frequency. This analysis illustrates the importance of matching both the Reynolds number and the reduced frequency of the insect and a laboratory model for proper scaling.

Discussing the forces in terms of lift and drag as used in conventional aerodynamics may not be as useful for flapping-wing flight. The forces that are important in flapping flight are the vertical component that balances the weight and the horizontal component that represents thrust/drag. These two components can be expressed using the lift and drag components, for the downstroke and upstroke, respectively, as

$$F_v = L_d\cos(\gamma_d) + D_d\sin(\gamma_d), \qquad F_h = L_d\sin(\gamma_d) - D_d\cos(\gamma_d) \tag{8}$$

$$F_v = L_u\cos(\gamma_u) - D_u\sin(\gamma_u), \qquad F_h = L_u\sin(\gamma_u) + D_u\cos(\gamma_u) \tag{9}$$

where L and D are perpendicular and parallel to the stroke plane, respectively. γ is the stroke plane inclination with respect to the horizontal. Subscripts d and u denote downstroke and upstroke, respectively.

Experimental Setup

We used two flat-plate wings made of Lucite (density = 1200 kg/m^3). The wing planform was a semi-ellipse with length-to-chord ratios (l_w/c), of 3 and 2, respectively, for wings designated W02 and W03. The wing root chords were 50 and 75 mm, respectively, and the thickness t was 2.1 mm for both wings. The wing edges were rounded using fine-grit sand paper. Torres and Mueller [8] have discussed the effect of edge radius on the dynamic vortex. The distance from the pivot point to the midpoint of the wing l_c was 0.260 m (10.25 in.). The pitching servomotor was mounted below the pivot, followed by the force transducer. One end of a 10-mm-diam rod was attached to the force transducer, and the wing was attached to the other end (Fig. 2). Relative to the wing length, the distance l_c is larger when compared with the corresponding distance to the wing rotation axis of natural fliers. Thus, the rotation effects can be expected to be slightly diminished in the present experiments. The limiting case for large values of l_c/l_w would correspond to plunging motion. This is an important distinction that must be considered when comparing the present results to those from natural fliers. The water in the tank was kept at a level such that the highest point on the wing at strokes extremities was about 1 cm below the water surface. The present flow visualization and force measurement experiments are with the wing operating in the LE/TE switching mode.

Flow Visualization

For the hydrogen bubble flow visualization experiments, the 75 × 150 mm^2 wing (W03) was used. The wing was painted flat black to reduce light reflection. The hydrogen bubble technique is described in our previous work [23]. The flow was illuminated with a microscope light with two fiber optic light guides. Images were acquired with a megapixel monochrome digital camera. End-view images were obtained by mounting a first surface mirror as shown in Fig. 2. The wing was flapped at a frequency $f = 0.115$ Hz. The corresponding Reynolds number was based on root chord and average velocity at midspan $Re_c = 4100$ and the corresponding reduced frequency $k = 0.138$. The angle of attack (α) was 30 deg. The images were acquired at a rate of 15 frames/s.

Force Measurements

A schematic of the present experimental setup is shown in Fig. 2. Figure 7 shows the servo timing diagram for pitch control. Figures 1–3 and 7 help describe the wing motion and discuss the results. Note in Figs. 3 and 7 the corresponding times during the stroke cycle given in terms of the period τ and the servo rotation time τ_s. Axes are also shown in Figs. 1–3 for ease of understanding of the flapping-and-pitching motions and the wing orientation. The timing of the servo actuation and the force transducer signal acquisition are controlled by National Instruments LabView software. The data acquisition board and a timer board are installed in the same computer. In Figs. 3 and 7, the indicated times are with reference to the zero displacement ($\xi = 0$) position. A typical sequence starts with powering up the dc motor to crank the wheel, Fig. 2. An encoder mounted on the DC motor shaft puts out an index pulse for time reference. Data acquisition begins when the encoder index pulse, generated once every revolution of the motor shaft, triggers the LabView data acquisition sequence. With the encoder index pulse as the time reference, LabView generates a pulse of appropriate delay, frequency, and duty cycle to trigger the servo at the desired instants shown in Figs. 3 and 7. The servo turns through angle 2α when this trigger pulse goes from low to high or high to low to get the desired orientations shown in Fig. 3.

The force transducer design requires careful consideration because of the low-level forces generated and their dynamic nature. A more detailed description of the present single-component force transducer design is given in our previous work [22]. For our single-component force transducer, a full Wheatstone bridge (Fig. 8) configuration is used to increase resolution and provide good dynamic response [29]. Because the design has temperature self-

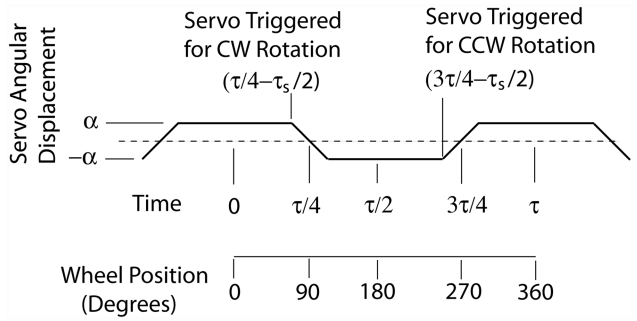

Fig. 7 Servo timing diagram, which along with Fig. 3, gives the relationship between the chord line (*AB*, Figs. 1 and 2) orientation and the servo actuation times during the stroke cycle, whose period τ and the servo rotation time τ_s are shown in both figures.

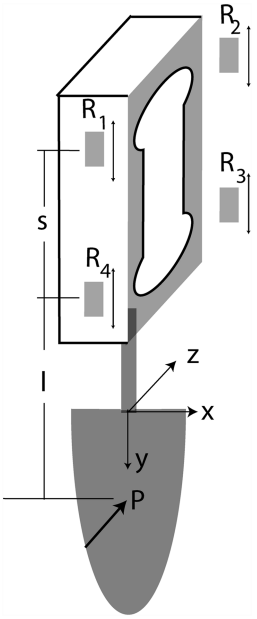

Fig. 8 Force transducer and wing. Four strain gauges are mounted symmetrically on opposite sides as shown.

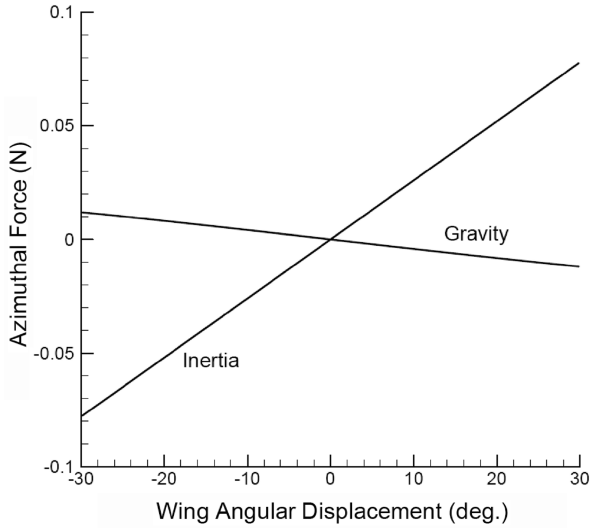

Fig. 9 Inertia and gravity forces on a 50 x 150 mm^2, semi-elliptical wing flapping in the vertical plane. Stroke angle ψ is 60 deg (Fig. 1). Frequency $f = 2$ Hz. Results from numerical quadrature of the equation of motion.

compensation, the readings are not affected by temperature swings. The force sensed by the transducer is independent of its point of application along the spanwise axis. In the present experiments, the wing was mounted to sense the force normal to the wing surface. Our analyses have shown that the tangential force along the wing surface due to skin friction will be <1% of the normal force. The voltage-resistance relationship for the Wheatstone bridge is discussed by Holman [29]. The bridge output voltage is independent of the distance to the point of application of the force P (Fig. 8). Therefore, this configuration can be used to measure the force without knowing the center of pressure location. Sensitivity can be increased by choosing an appropriate material and geometry, but limiting the maximum strain well below the gauge's fatigue limit.

The force transducer dynamic range can be improved by proper choice of the strain gauge and by designing for the expected load range. The present force transducer specifications are as follows: nominal rated output is 2 mV/V; zero balance is 3% rated output; nominal bridge resistance is 1000 Ω; nonlinearity is ±0.05% rated output; hysteresis is ±0.05% rated output; creep is ±0.05% load; and mass is 30 g. The transducer was designed for a maximum load of 1 N. The signal was processed through a signal conditioner/amplifier and filtered using a lowpass filter with the cutoff frequency set at 3 Hz. The filtered output was input into LabView for storage and processing; it was also monitored on an oscilloscope. The transducer was calibrated statically using weights. To ascertain if the point of application of the force in the spanwise direction has any influence on the output, tests were repeated by placing the weight at different spanwise locations and monitoring the output. No differences were observed within the accuracy of the digital voltmeter display. Calibration was repeated after the experiments were completed to detect any drift. The calibration constants obtained before and after the experiments spanning three months differed only by 0.3%.

Experimental Uncertainty Analysis

The flapping-and-pitching wing experiment using small wings as in the present study has some unique challenges posed by the low force levels (~1 N) and the cyclic wing motion. The low force levels require careful selection and/or design of transducers that will ensure good signal-to-noise ratio. Wing motion introduces systematic errors that must be accounted for. Depending on the experiment configuration and force transducer placement, gravity and inertia forces may contribute to the signal. Because of these concerns, a systematic error analysis is necessary to establish error bars for the data. Using wings of different materials and repeating the experiments in air are two ways in which wing inertia forces can be estimated and subtracted from the force sensed by the transducer. It is also possible to calculate the forces due to inertia and gravity by analytical/numerical calculations. We have written a computer program for this purpose. For a wing having uniform mass distribution along the length, the inertia and gravity force terms may be calculated as, respectively, the first and the second term on the right-hand side of the following equation:

$$F_\xi = \rho_{\text{wing}} A \omega^2 \frac{l_w^2}{2} \xi - g \rho_{\text{app}} A l_w \sin \xi \tag{10}$$

where $\rho_{\text{app}} = \rho_{\text{wing}} - \rho$, the apparent density of the wing. For a wing with variable mass distribution, the force must be calculated by numerical quadrature.

A sample result from the numerical calculations is shown in Fig. 9 for a semi-elliptic wing in harmonic motion. (See Fig. 2 for the stroke plane XY in which the motion takes place. Gravity is in the Y direction.) When pitching is present, the inertia and weight components in the z direction must be calculated for each orientation the wing sees during the cycle. For a wing flapping in the horizontal plane, the weight contribution does not change during the stroke cycle, and it can be easily subtracted from the transducer output signal. For a wing translating in the vertical plane in the plunge-pitch mode, weight will not influence transducer response in our design. For a pitching wing with a pitch axis different from an axis of symmetry, additional inertia forces must be considered. This can also be done through calculations or by doing the experiment in air and subtracting the result from the water experiment. Equation (10) shows the square dependence of the flapping frequency f on the inertia force. Plunging and flapping-wing experiments have been reported for f values up to 30 Hz, at which the inertia force will be 225 times greater than that at 2 Hz, which shows that not accounting for inertia force will introduce large errors at the higher frequencies.

Electronic noise is another source of error in transducers. Electrical wires were shielded, and other recommended practices followed as much as possible to reduce noise. A low-pass filter with cutoff frequency equal to 10 times the flapping frequency, well above the Nyquist limit, can be used to increase signal-to-noise ratio. Effect of water tank walls, another potential source of error, can be minimized by having a tank large enough such that the tank side walls are at least 6 chord lengths away from the wing. The bottom wall also should be sufficiently far from the wing tip. In the present experiments, the bottom wall was two wing lengths away from the wing tip. One way to alleviate the error introduced by free surface

waves is to cover the surface by a rigid wall to prevent surface wave formation. We have determined, by observing light reflections from the water surface, that no significant wave motion was generated in the present experiments. Wave effects are confined within a relatively shallow layer near the free surface given by the relation $h < \lambda/2$, where h is the depth and λ is the wavelength of the free-surface wave [30]. Because the depth h is not constant in the present experiments, a more detailed analysis of free surface effects would be quite involved, and hence not attempted in this work. However, it is our goal to perform such analyses in future studies. Additional sources of error include out-of-plane motion of the wing, flexure of the wing-rod-mounting bracket assembly, and errors in synchronizing the flapping-and-pitching motion, estimated to be a maximum of ± 15 ms. We estimate that, after correcting for the systematic errors due to weight and inertia, the remaining errors introduce a total of $\sim \pm 10\%$ uncertainty in the presented force data.

Results

Flow Visualization

The eight frames in Fig. 10 were acquired by pointing the camera in the end-view direction shown in Fig. 2, which should be used to interpret the images. These eight frames are for $\alpha = 30$ deg for different orientations of the wing during pitching at the left end of the stroke. The consecutively numbered frames are 67 ms apart. The meaning of leading-edge/trailing-edge switching can be understood

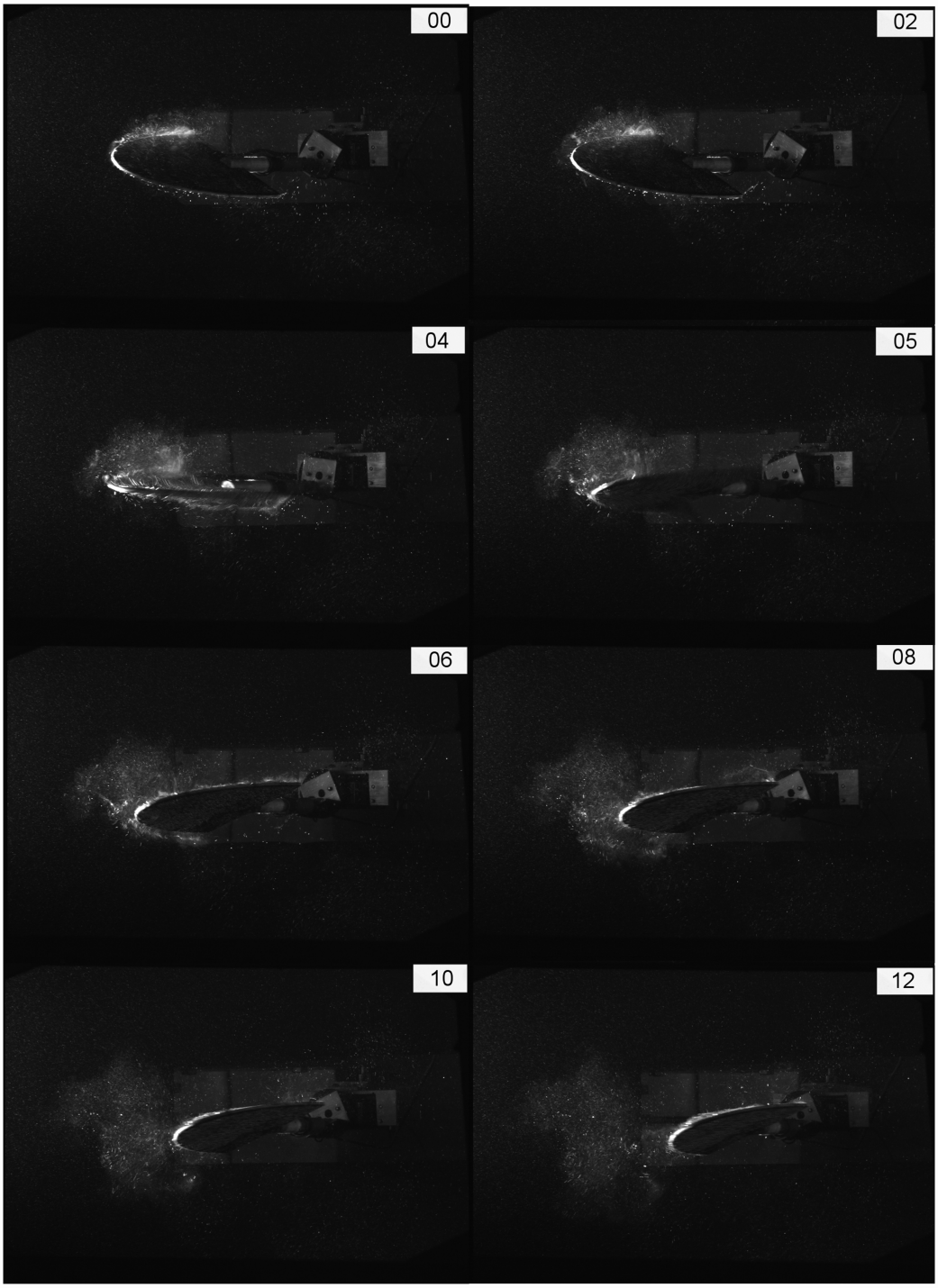

Fig. 10 $\alpha = 30$ deg, $Re_c = 4100$, $k = 0.138$. These eight frames show the wing in end view (Fig. 2) during pitching. In this view, the rotation is counterclockwise. These eight frames cover the time in which the wing reaches the left extremity and reverses direction.

from Fig. 10; when the wing rotation is completed, the leading edge from the previous half-stroke becomes the trailing edge, and the trailing edge from the previous half-stroke is now the leading edge. The frames are chosen to show the dynamic nature of the flowfield. Frames 01, 03, 07, 09, and 11 are omitted because they do not contain any significant additional flow features, thus helping to reduce the number of frames needed for the discussion. Frame 00, captured just before stroke reversal, shows the leading-edge vortex that is stronger toward the wing root. Frame 02 is also shown before pitching begins at stroke reversal. The features are similar to those in frame 00. The leading-edge vortex that can be seen in frames 00 and 02 is designated vortex A for the discussion here. Frame 04 shows features that have developed during pitching. Two vortices at the two edges are now clearly visible; one is vortex A, which has transformed significantly by the wing rotation, and a second vortex, designated vortex B, has formed at the other edge. In frame 05, the structure has changed significantly from frame 04. Vortex A has acquired a more three-dimensional structure. Vortex B appears to have dissipated almost completely, because it is hardly visible and has moved downstream. In frames 06, 08, and 10, vortex A gradually moves outward and away from the wing. At the same time, a new leading-edge vortex can be seen to form even though the leeward side of the wing is now hidden from view. The spanwise motion of vortex A is of great interest because its direction is toward the wing tip, the opposite of what happens on a fixed wing at high α. This observation has also been made by Usherwood and Ellington [7].

Force Data

The wing was flapped about the pivot axis (Z axis) shown in Figs. 1 and 2 at frequencies in the range 0.22–0.30 Hz and a nominal stroke angle (see Fig. 1) $\psi = 60$ deg. For all the present cases, the wing was pitched at a constant angular velocity $\omega = 5.236$ rad/s. The pitching was symmetrical about the stroke extremities, and at the end of the pitching motion, the wing assumed a constant angle-of-attack orientation with respect to the stroke plane. Figure 3 shows, in end view, the orientation of the chord line AB (shown in Figs. 1 and 2) at different points in the stroke cycle. The two darker gray end regions in Fig. 3 indicate pitching phase and the lighter middle region indicates constant orientation with respect to the stroke plane. The time intervals for the different phases of the wing motion are given in terms of the period τ of the stroke cycle, and the servo operation time τ_s. These time intervals are also shown in the servo timing diagram in Fig. 7.

Force measurement experiments were run at two angles of attack, $\alpha = 30$ and 45 deg. To estimate the extent of deviations from symmetry between the downstroke and upstroke, and the effect on the transducer force output when the loading direction was reversed, the experiments were repeated for all the present cases, with α being negative during the downstroke (Fig. 3) and positive during the upstroke. Except for the transducer signal changing sign, no significant differences were noticeable.

Figure 11 shows the instantaneous fluid dynamic force during one complete cycle for $\alpha = 30$ deg at two flapping frequencies, 0.22 Hz (Fig. 11a) and 0.29 Hz (Fig. 11b). Figure 12 shows results at the same two frequencies for $\alpha = 45$ deg. The reduced frequency $k = 0.092$ for all four cases. These results were obtained after applying analytically determined corrections for inertia and weight, as described in the Experimental Uncertainty Analysis section. These are three-run averages for one stroke cycle taken from transducer signals acquired at a data sampling rate of 1 kHz over an ~30-s duration. The signals showed good cycle-to-cycle repeatability with a maximum of 4% difference in the peak values. The shaded vertical bars indicate the 0.2-s duration of servo rotation. The region between the first and the second shaded bars is named downstroke, and the following one is named upstroke. For pure harmonic flapping motion with pitching symmetry about the stroke end points, one might expect symmetry between the downstroke and upstroke forces. The four plots in Figs. 11 and 12 indicate some degree of asymmetry. This may be due to a number of reasons, inaccuracies in servo synchronization being one. The flapping motion was only near harmonic, as was determined from an analysis of the kinematics. Though not detectable in simple visual observations, there might exist a certain degree of out-of-plane motion during the stroke cycle. Even though the previously mentioned factors might have introduced asymmetry, overall, the differences between the two halves of a full cycle are not significant. Quantitative video analysis that can be used to estimate these errors will be considered for future implementation. The force $\bar{F}$ normal to the wing shown in Figs. 11 and 12 is a three-run average for one stroke cycle. It is resolved as follows to calculate lift and drag:

$$L = \bar{F}\cos\alpha \quad \text{and} \quad D = \bar{F}\sin\alpha \tag{11}$$

The lift coefficient C_L and the drag coefficient C_D are defined as

$$C_L = \frac{L}{\bar{q}S} \quad \text{and} \quad C_D = \frac{D}{\bar{q}S} \tag{12}$$

The force peak in Fig. 11a is about 0.15 N. The downstroke peak on the left and the upstroke peak are nearly at the same level. The force can be seen to follow the velocity variation, which has a maximum when the wing is vertical, where the angular displacement $\xi = 0$. We have chosen to use the forces instead of the coefficients in

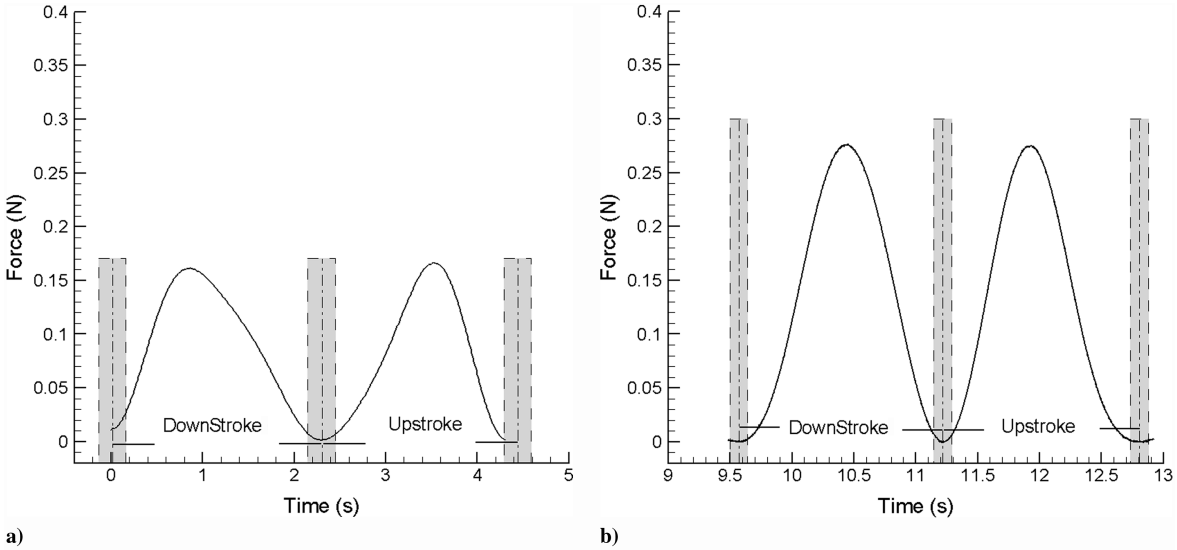

Fig. 11 Force normal to the wing, W02. Chord = 50 mm, $\alpha = 30$ deg, $k = 0.092$ for a) and b). The shaded vertical bars indicate pitching phase with $\tau_s = 0.2$ s. a) $f = 0.22$ Hz; b) $f = 0.29$ Hz.

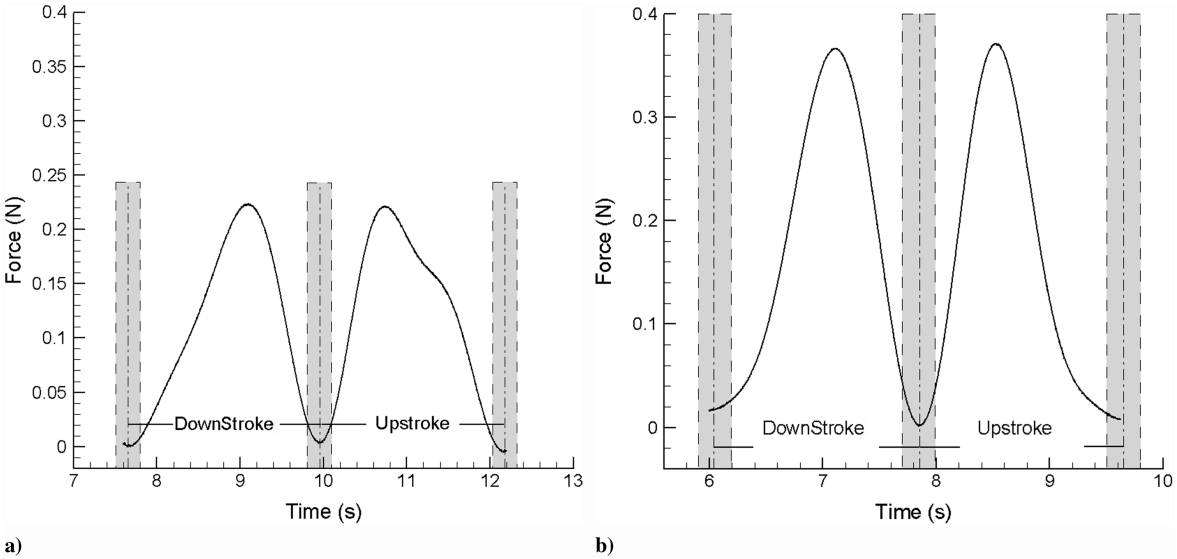

Fig. 12 Force normal to the wing, W02. Chord = 50 mm, $\alpha = 45$ deg, $k = 0.092$ for a) and b). The shaded vertical bars indicate pitching phase with $\tau_s = 0.2$ s. a) $f = 0.22$ Hz; b) $f = 0.29$ Hz.

Figs. 11 and 12 for other researchers to more directly compare their data with the present results. As can be seen from Eqs. (3), (11), and (12), the instantaneous force in Figs. 11 and 12, and the corresponding C_L scale by a constant factor; therefore, the instantaneous C_L values can be easily calculated using the known values of l_c, S, ψ, f, and α. As expected, at the two end-of-stroke locations, where the speed is zero, the fluid dynamic force also is near zero. The average lift coefficient $C_L = 1.68$ for the case in Fig. 11a, obtained by numerical integration of the force results. The C_L values are of the same order as in previous studies. However, a more direct comparison of the values from different studies is difficult because of the differences in the nondimensionalization schemes used to define force coefficients. To illustrate, C_L will be reduced by ~40% if the tip mean speed is used to calculate the dynamic pressure instead of the midpoint mean speed. Of the four plots in Figs. 11 and 12, those for the higher frequency $f = 0.29$ Hz have better symmetry between the downstroke and the upstroke compared with those for the lower flapping frequency. This may be due to the force transducer, rated for 1-N force, operating in a more optimal range. Figure 12a force variation for the upstroke has a shoulder not seen in the other plots. This was observed in all the cycles of the runs to which it belongs. It is probably caused by a slight asymmetry in the pitching motion. However, this needs to be further investigated with more experiments under the same conditions. The trends in the force magnitudes are as expected. Force levels are higher for the higher angle of attack and higher flapping frequency.

The shape of the force curve in the present study is quite different from those in previous studies. Dickinson et al. [15] have a flatter profile for the force variation compared with the present results. These differences can likely be attributed to the differences in the motion profile. The angular displacement of the flapping motion in the present work is near sinusoidal, which is different from the motion profile used by Dickinson et al. [15]. We also employed LE/TE switching between the two halves of the stroke cycle (see Fig. 3), which is an aspect of the present study that is not biologically inspired. To completely understand the effect of this mode of pitching motion on force generation, a larger parameter space must be considered. However, the present C_L values suggest that LE/TE switching does not introduce any performance degradation; on the other hand, in the absence of dynamic camber variation such as employed by many hovering insects, wings with fixed nonzero camber can be used only with LE/TE switching. Other preliminary studies have recently appeared showing, with the help of CFD simulations of elliptic cross-section airfoils, that LE/TE switching results in substantial increase in average c_1, indicating that, though not a desirable airfoil section for MAV, the elliptic cross-section airfoil performs better in the LE/TE switching mode. Clearly, additional studies are necessary to firmly establish the advantages/disadvantages of LE/TE switching. We have carefully avoided using data belonging to the first and the last few cycles from each run to eliminate starting and stopping effects. The two-dimensional results of Sunada et al. [31] for a plunging-and-pitching airfoil provide a source to qualitatively compare the present results. After allowing for the differences in the nondimensionalization schemes, their force coefficient seems to be much larger than the present values.

Based on the collective results from our studies, a vortex-trapping model for force enhancement in the LE/TE switching mode has been proposed [23]. Unsteady flow interacting with a moving surface such as the present can be studied as vortex interaction with a solid surface. Rockwell's review [32] covers studies of parallel, streamwise, and perpendicular vortices interacting with a surface such as the leading edge of an airfoil, and Yavuz and Rockwell [33] used critical point theory to analyze three-dimensional, vortex-dominated flowfield about delta wings. The two-dimensional interactions provide a means to calculate the unsteady forces induced on the surface by the vortex and the subsequent distortion of the vortex itself. Considering how rapidly the vortices diffuse [19], a simple model that includes only one vortex in the interaction might be sufficient to account for most of the effects. The flow physics underlying the two previously proposed concepts [19,22,23], LE/TE switching and frequency tuning, can both be understood in terms of vortex-body interactions. The schematic in Fig. 13 would help explain the underlying phenomena. Toward the end of the downstroke, a trailing-edge vortex (TEV) forms, as shown on the left-hand side of the Figure. At stroke reversal, the previously formed TEV having the counterclockwise sense is now at the leading edge, resulting in an increment in the force ΔF_{TEV}. Note that the vortex interaction in Fig. 13 is the parallel type [32].

Gopalkrishnan et al. [10] have shown that propulsive efficiency of a foil moving in the wake of a Karman street is dependent on the distance from the body producing the vortex street and the proximity of the foil's encounter with the vortices in the street, determined by the phase angle of the foil motion. It is not clear if the interaction shown in Fig. 13 is the same type as in the study mentioned previously because of the alternating sense of rotation of their vortices the foil sees in the Karman street. As in the experiments of Gopalkrishnan et al. [10], the vortices in the wake decay fast in the present case. LE/TE switching can, therefore, be seen to be helpful in exploiting the TEV from the previous half-stroke ($\mathrm{TEV}_{\mathrm{ds}}$, Fig. 13) at the optimum instant in its evolution. This description of the vortex-foil interaction suggests methods for flow control. Implementing passive flow control by using data from phase-locked flow

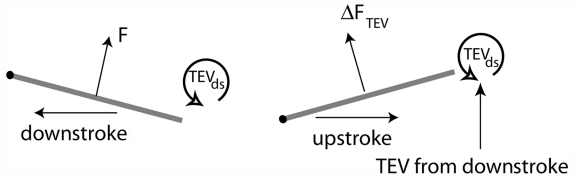

Fig. 13 A vortex-trapping model for lift augmentation due to the trailing-edge vortex (TEV) from the previous half-stroke.

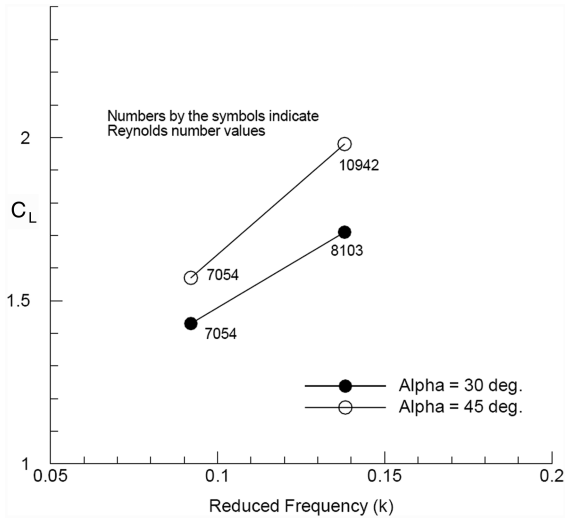

Fig. 14 Effect of reduced frequency on average lift coefficient calculated by numerically integrating the measured force.

visualization and particle image velocimetry (PIV) would be one way to do this. Velocity vector- and vorticity-field data from PIV images can be used to quantify the forces created during the vortex-surface interaction. The vortex-trapping model shown in Fig. 13 is equally applicable for cambered plate airfoils.

Ten experiments with the following parameter variations were run: $l_w/c = 3, 2$; $\alpha = 30, 45$ deg; Re_c range $= 5400–10,900$; and reduced frequency $k = 0.092, 0.138$. Even though varying only one parameter at a time was preferable, experimental limitations did not allow this approach. The results from these runs point to the trends with respect to reduced frequency. The experiments also afforded a test for our previous suggestion [19] that an optimum reduced frequency might exist around 0.22. Sample average C_L results for k values of 0.092 and 0.138 plotted in Fig. 14 show an increasing trend with increasing value of k. However, further experiments are needed to determine the optimum k value, if it exists.

Conclusions

The present simulation and experimental results shed much light on the unsteady flow features of a flapping-and-pitching wing. Techniques such as leading-edge/trailing-edge switching and frequency tuning, proposed previously by us, are further explored in the present work. The experimental work was initiated to further seek validity for the suggested mechanisms. The present results show that the force curve for the stroke cycle closely follows the velocity profile. The flat-plate wing of semi-elliptic planform undergoing near-harmonic flapping motion and pitching about the axis of symmetry does not produce end-of-stroke peaks and troughs in the force curve. The results show that LE/TE switching makes it feasible to use insect/birdlike cambered wings to increase performance when dynamic camber control is not feasible. This is a significant finding because of its implications in airfoil selection. A vortex-trapping model that explains force augmentation in the LE/TE switching mode is proposed.

Experimental investigation of another previous suggestion, that frequency tuning may lead to enhanced performance, was done at two reduced frequencies, 0.092 and 0.138. The results show larger C_L values at the higher value of k, indicating that an optimum in the neighborhood of 0.22 might exist as proposed. The experimental setup is presently being modified to cover a wider range of reduced frequencies.

Systematic and random errors in the data are discussed, and analytically determined corrections have been applied for the systematic errors due to wing inertia and weight. Care was taken to select force transducer parameters appropriate for the low force levels ($\sim$1 N). Overall experimental uncertainty due to other factors such as electrical noise, imperfections in apparatus fabrication and assembly, and deviations from the design motion profile has been estimated.

Ongoing and immediate future work includes investigation of a range of reduced frequencies; use of cambered plate airfoils; flowfield investigation using particle image velocimetry; CFD simulations of low Reynolds number, high angle-of-attack wings; using critical point theory to analyze the three-dimensional flowfields; and investigation of other motion profiles for flapping as well as pitching.

Acknowledgments

This work was sponsored by the NASA Institute for Advanced Concepts (NIAC), Ohio Aerospace Institute (OAI), main contractor. Our special thanks to Robert Cassanova, NIAC Director, for project funding and his keen interest in the entomopter and solid state aircraft projects. J. Rolwes was partially supported by a NASA Space Grant Consortium Fellowship. The authors wish to acknowledge many productive discussions with Mohsen Shahinpoor, Phillip Jenkins, Dave Olinger, Teryn DalBello, Pavan Shivaram, Curtis Smith, Terri Deacey, Raja Banerjee, and Taylor Swanson.

References

[1] "Planetary Exploration using Biomimetics: An Entomopter for Flight on Mars," NASA Institute for Advanced Concepts (NIAC), Ohio Aerospace Institute, Project Final Report OAI-2002-NIAC-01, Oct. 2002.

[2] "Solid State Aircraft," NASA Institute for Advanced Concepts (NIAC), Ohio Aerospace Institute, Project Final Report OAI-2005-NIAC-02, May 2005.

[3] *Fixed and Flapping Wing Aerodynamics for Micro Air Vehicle Applications*, edited by T. J. Mueller, Progress in Astronautics and Aeronautics, Vol. 195, AIAA, Reston, VA, 2001.

[4] Mueller, T. J., and DeLaurier, J. D., "Aerodynamics of Small Vehicles," *Annual Review of Fluid Mechanics*, Vol. 35, Jan. 2003, pp. 89–111. doi:10.1146/annurev.fluid.35.101101.161102

[5] Sane, S. P., "The Aerodynamics of Insect Flight," *Journal of Experimental Biology*, Vol. 206, No. 23, 2003, pp. 4191–4208. doi:10.1242/jeb.00663

[6] Ellington, C. P., "The Novel Aerodynamics of Insect Flight: Applications to Micro-Air Vehicles," *Journal of Experimental Biology*, Vol. 202, No. 23, 1999, pp. 3439–3448.

[7] Usherwood, J. R., and Ellington, C. P., "The Aerodynamics of Revolving Wings I. Model Hawkmoth Wings," *Journal of Experimental Biology*, Vol. 205, 2002, pp. 1547–1564.

[8] Torres, G. E., and Mueller, T. J., "Low Aspect Ratio Wing Aerodynamics at Low Reynolds Numbers," *AIAA Journal*, Vol. 42, No. 5, 2004, pp. 865–873.

[9] Freymuth, P., "Propulsive Vortical Signature of Plunging and Pitching Airfoils," *AIAA Journal*, Vol. 26, No. 7, 1988, pp. 881–883.

[10] Gopalkrishnan, R., Triantafyllou, M. S., Triantafyllou, G. S., and Barrett, D., "Active Vorticity Control in a Shear Flow Using a Flapping Foil," *Journal of Fluid Mechanics*, Vol. 274, 1994, pp. 1–21. doi:10.1017/S0022112094002016

[11] Anderson, J. M., Streitlien, K., Barrett, D. S., and Triantafyllou, M. S., "Oscillating Foils of High Propulsive Efficiency," *Journal of Fluid Mechanics*, Vol. 360, 1998, pp. 41–72. doi:10.1017/S0022112097008392

[12] Lewin, G. C., and Haj-Hariri, H., "Modelling Thrust Generation of a Two-Dimensional Heaving Airfoil in a Viscous Flow," *Journal of Fluid Mechanics*, Vol. 492, 2003, pp. 339–362. doi:10.1017/S0022112003005743

[13] Lewin, G. C., and Haj-Hariri, H., "Reduced-Order Modeling of a Heaving Airfoil," *AIAA Journal*, Vol. 43, No. 2, Feb. 2005, pp. 270–283.
[14] Koochesfahani, M. M., "Vortical Patterns in the Wake of an Oscillating Airfoil," *AIAA Journal*, Vol. 27, No. 9, Sept. 1989, pp. 1200–1205.
[15] Dickinson, M. H., Lehmann, F., and Sane, S. P., "Wing Rotation and the Aerodynamic Basis of Insect Flight," *Science*, Vol. 284, June 1999, pp. 1954–1960.
doi:10.1126/science.284.5422.1954
[16] Tarascio, M. J., Ramasamy, M., Chopra, I., and Leishman, J. G., "Flow Visualization of Micro Air Vehicle Scaled Insect-Based Flapping Wings," *Journal of Aircraft*, Vol. 42, No. 2, 2005, pp. 385–390.
[17] Vest, M., and Katz, J., "Unsteady Aerodynamic Model of Flapping Wings," *AIAA Journal*, Vol. 34, No. 7, 1996, pp. 1435–1440.
[18] Ramamurti, R., and Sandberg, W. C., "A Three-Dimensional Computational Study of the Aerodynamic Mechanisms of Insect Flight," *Journal of Experimental Biology*, Vol. 205, 2002, pp. 1507–1518.
[19] Isaac, K. M., Shivaram, P., and DalBello, T., "Low Re, High α Aerodynamics with Controlled Wing Kinematics," AIAA Paper 2003-4019, 2003.
[20] Lentink, D., and Gerritsma, M., "Influence of Airfoil Shape on Performance in Insect Flight," AIAA Paper 2003-3447, 2003.
[21] Taylor, G. K., Nudds, R. L., and Thomas, A. L. R., "Flying and Swimming Animals Cruise at Strouhal Number tuned for High Power Efficiency," *Nature (London)*, Vol. 425, Oct. 2003, pp. 707–711.
doi:10.1038/nature02000
[22] Isaac, K. M., Colozza, A., and Rolwes, J., "Force Measurements on a Flapping and Pitching Wing at Low Reynolds Numbers," AIAA Paper 2006-0450, 2006.
[23] Isaac, K. M., Rolwes, J., and Colozza, A., "Unsteady Flow Features of a Flapping and Pitching Wing at Low Reynolds Number," AIAA Paper 2006-3145, 2006.
[24] FLUENT Computational Fluid Dynamics Software Package, Ver. 6.3, FLUENT, Inc., Lebanon, NH, 2002.
[25] Issa, R. I., "Solution of Implicitly Discretized Fluid Flow Equations by Operator Splitting," *Journal of Computational Physics*, Vol. 62, No. 1, 1986, pp. 40–65.
doi:10.1016/0021-9991(86)90099-9
[26] Cloupeau, M., Devillers, J. F., and Devezeaux, D., "Direct Measurement of Instantaneous Lift in Desert Locust; Comparison with Jenson's Experiments on Detached Wings," *Journal of Experimental Biology*, Vol. 80, 1979, pp. 1–15.
[27] White, F. M., *Viscous Fluid Flow*, 2nd ed., McGraw–Hill, New York, 1991.
[28] Kunz, P. J., and Kroo, I., "Analysis and Design of Airfoils for Use at Ultra-Low Reynolds Numbers," *Fixed and Flapping Wing Aerodynamics for Micro Air Vehicle Applications*, edited by T. J. Mueller, Vol. 195, Progress in Astronautics and Aeronautics, AIAA, Reston, VA, 2001.
[29] Holman, J. P., *Experimental Methods for Engineers*, 7th ed., McGraw–Hill, New York, 2001, Chap. 10.
[30] Newman, J. N., *Marine Hydrodynamics*, MIT Press, Cambridge, MA, 1977, Chap. 6.
[31] Sunada, S., Kawachi, K., Matsumoto, A., and Sakaguchi, A., "Unsteady Forces on a Two-Dimensional Wing in Plunging and Pitching Motions," *AIAA Journal*, Vol. 39, No. 7, 2001, pp. 1230–1239.
[32] Rockwell, D., "Vortex-Body Interactions," *Annual Review of Fluid Mechanics*, Vol. 30, Jan. 1998, pp. 199–229.
doi:10.1146/annurev.fluid.30.1.199
[33] Yavuz, M. M., and Rockwell, D., "Control of Flow Structure on Delta Wing with Steady Trailing Edge Blowing," *AIAA Journal*, Vol. 44, No. 3, 2006, pp. 493–501.

F. Coton
Associate Editor